nature photonics

SUPPLEMENTARY INFORMATION
https://doi.org/10.1038/s41566-019-0397-3

In the format provided by the authors and unedited.

Femtofarad optoelectronic integration demonstrating energy-saving signal conversion and nonlinear functions

Kengo Nozaki[1,2*], Shinji Matsuo[1,3], Takuro Fujii[1,3], Koji Takeda[1,3], Akihiko Shinya[1,2], Eiichi Kuramochi[1,2] and Masaya Notomi[1,2*]

[1]Nanophotonics Center, NTT Corporation, Atsugi, Japan. [2]NTT Basic Research Laboratories, NTT Corporation, Atsugi, Japan. [3]NTT Device Technology Laboratories, NTT Corporation, Atsugi, Japan. *e-mail: kengo.nozaki.fd@hco.ntt.co.jp; masaya.notomi.mn@hco.ntt.co.jp

1. Device design and fabrication

The design of the other PhC parameters for the PhC-PD and the PhC-EOM are shown in Figure S1. The lattice constant *a* for the PhC-PD and the PhC-EOM are 440 nm and 430 nm, respectively. The airhole diameter 2*r* is approximately 200 nm. The design of the airhole shifts S_a, S_b, and S_c for the L3 nanocavity is taken from Ref. 1 and 2. InGaAsP with an absorption wavelength of 1.48 μm and a length of 1.3 μm is embedded in a nanocavity of the PhC-EOM. The same type of L3 nanocavity design was investigated for our previous paper, and the theoretical Q of more than 10^5 and the experimental Q of more than 10^4 have been reported [2]. In the same report, we estimated the standard deviation of 0.54 nm for the resonant wavelength fluctuation. An InGaAs absorber is embedded for the PhC-PD. Because of the index difference between the input InP waveguide and the InGaAs-embedded waveguide, their widths should be adjusted so that their guiding bands match. To this end, the waveguide widths of the InP and InGaAs(P)-embedded regions were changed to $1.12W_0$ and $0.95W_0$, respectively, where $W_0 = \sqrt{3}a$ is the basic line defect width defined as the removal of one row of airholes.

For the fabrication, we used a semi-insulating InP substrate and grew a 1-μm thick InAlAs sacrificial layer, a 156-nm thick InGaAsP layer (as a nonlinear material for EOM), and a 30-nm thick InP cap layer by employing metal–organic chemical vapor deposition (MOCVD). Through the patterning/etching of the InGaAsP region and the regrowth of a 20-nm-thick InP buffer and a 143-nm-thick InGaAs layer, which is based on our buried-heterostructure (BH) regrowth technique[3], an InGaAsP region and an InGaAs region were formed separately in the substrate. The small absorption region of the InGaAsP and InGaAs for EOM and PD, respectively, were simultaneously defined with a SiN mask using electron-beam (EB) lithography and were embedded in undoped InP by the same BH regrowth procedure. Si ion implantation and Zn thermal diffusion were carried out for n-doping and p-doping, respectively, thus forming a lateral p-i-n junction in the undoped-InP layer. The photonic-crystal airholes were formed by using EB lithography and Cl_2-based dry etching. Metallization was carried out for the electrical contact and wiring with electrode pads. Finally, an air-bridge structure was formed by wet etching.

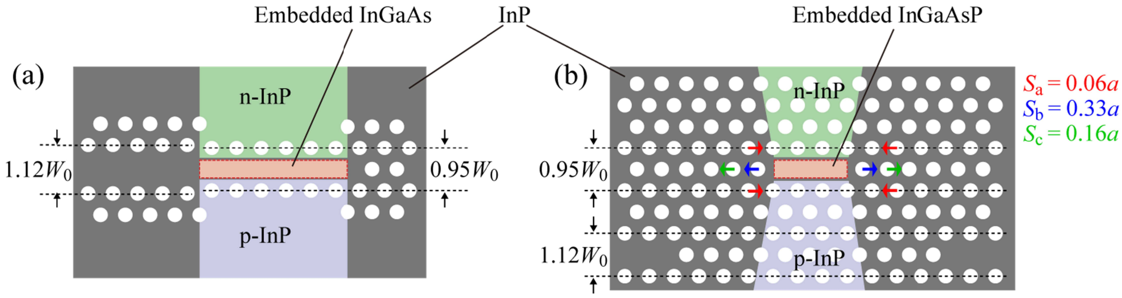

Figure S1 Device design. (a) PhC-PD, (b) PhC-EOM.

2. Measurement setup and dynamics for single PhC-EOM

We measured the electrical and optical responses for an applied DC voltage to evaluate the static characteristics of the single PhC-EOM. Figure S2(a) shows I-V curves for the forward bias voltage region of the p-i-n junction.

The resonant optical transmission was also measured as shown in Figure S2(b), which is the same as Fig. 1(b) in the main text. The same type of L3 nanocavity design was investigated for our previous paper, and the theoretical Q of more than 10^5 and the experimental Q of more than 10^4 have been reported [2]. For the EOM in this paper, the cavity *Q* depends on the material absorption of the embedded InGaAsP. The absorption wavelength (1.48 μm) of the InGaAsP should be moderately close to the operation wavelength (1.546 μm) for the enhancement of the EO nonlinearity. This resulted in the moderate cavity *Q* of 5400. The maximum resonant transmission was observed at a forward voltage of +0.7 V because of the elimination of the built-in voltage of the p-i-n junction and the consequent suppression of the FKE. The on-chip optical loss at this voltage was 2.3 ± 0.6 dB, which was estimated by comparing the output power with that of a reference waveguide fabricated on the same chip.

The PhC-EOM was also dynamically driven by applying an AC signal voltage combined with a DC bias voltage via a bias tee. We used an RF probe with a 50 Ω termination to realize impedance matching with the signal generator and thus eliminate the signal back reflections and accurately estimate the applied voltage across the EOM. (Note that the 50-Ω termination will not be required when the EOM is integrated with a CMOS driver circuit appropriately designed for impedance matching.) The wavelength and power of the incident light were fixed at 1546.6 nm and –10 dBm, respectively. Figure S2(c) shows the eye diagrams for bit rates of 40 Gbit/s and 10 Gbit/s. In this measurement, a forward bias voltage V_{bias} = 0.4 V and a signal voltage V_{pp} = 0.5 V were applied (The swing voltage ranges from +0.15 V to +0.65 V in the forward voltage region). An NRZ optical signal with a 2^{11}−1 PRBS frame was repeatedly injected, and 128 frames were averaged to exclude the intrinsic electrical noise of the oscilloscope sampling head.

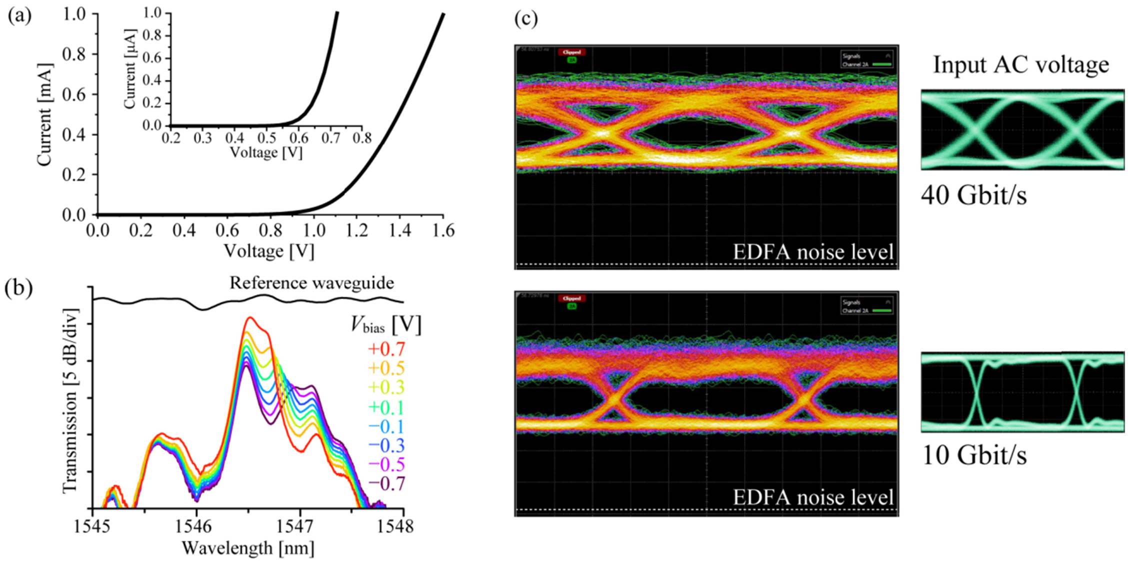

Figure S2 Measurement results for a single EOM. (a) I-V curve for the forward bias voltage region. The inset shows a magnified curve of the voltage below +0.7 V. (b) Transmission spectra for different bias voltages (Same as Fig. 1(b) in the main text). (c) Eye diagrams for bit rates of 40 Gbit/s and 10 Gbit/s. The incident light wavelength is 1546.6 nm. A forward bias voltage of V_{bias} = +0.4 V and a signal voltage of V_{pp} = 0.5 V are applied.

3. Energy consumption for single PhC-EOM

The intrinsic energy consumption required for PhC-EOM originates from (i) the dissipation energy generated by charging and discharging the device capacitance (E_{ch}) and (ii) the dissipation energy generated by the current flow under an external voltage (E_{ext})[4-6], and each contribution is estimated as follows.

Our PhC-EOM has a theoretical capacitance of only C_{EOM} = 0.6 fF. When considering V_{pp} = 0.5 V for the dynamic modulation, the required charge for the capacitance during the modulation is given by $\Delta Q_{EOM} = C_{EOM}V_{pp}$ = 300 aC. There is on average one complete charge/discharge cycle every 4 bits in the random bit sequence of an NRZ signal, and E_{ch} is thereby given by $\Delta Q_{EOM}V_{pp}/4$, and accordingly, the dissipation energy consumed by charging the capacitance (i) is ~ 40 aJ/bit.

On the other hand, the current supply from the external reverse voltage source results in the energy consumption E_{ext}. This is given by $(I_{on}V_{on} + I_{off}V_{off})/2f_{mod}$, where V_{on}, I_{on} and V_{off}, I_{off} are the bias voltages and currents in the on and off states, and f_{mod} is the modulation bit rate. We applied a swing voltage in the +0.15 V to +0.65 V range in the forward voltage region for the dynamic modulation seen in Figure S2(c). The corresponding current swing was estimated from the I-V curve in Figure S2(a), and was from 100 pA to 250 nA. Accordingly, the dissipation energy caused by the external voltage (ii) is ~ 2 aJ/bit and ~ 8 aJ/bit for bit rates of 40 and 10 Gbit/s, respectively. These values are much smaller than the charging energy consumption.

For the electro-absorption modulator, the dissipation energy generated by the photo-generated current and external voltage should also be considered[4,7]. However, the photocurrent dissipation energy is consumed only in the reverse voltage range, and completely eliminated for a forward-biased modulation such as our experiment. Consequently, we conclude that the total energy consumption of a single PhC-EOM is only 42 aJ/bit for a 40 Gbit/s modulation.

4. Simulated capacitance and frequency response of O-E-O transistor

The capacitance of the integrated device is calculated with the three-dimensional finite-element method (FEM). Figure S3(a) shows the simulation model, including the PD-EOM and electrode pads with a 30×30 μm^2 area. Figure S3(b) and (c) show the simulation results, which are separately calculated for the PD and EOM, respectively. The theoretical capacitances are C_{PD} = 0.85 fF for the PD and C_{EOM} = 0.79 fF for the EOM, hence giving a total capacitance $C = C_{PD} + C_{EOM}$ = 1.64 fF. The simulation also gives a pad-to-pad capacitance of about 5 fF. However, it works as a bypass capacitance and does not affect the local high-speed response of the PD-EOM[8]. This is confirmed in the simulated frequency response of the transimpedance, as shown later. In addition, the large electrical pad should be removed when the device is actually integrated on a chip.

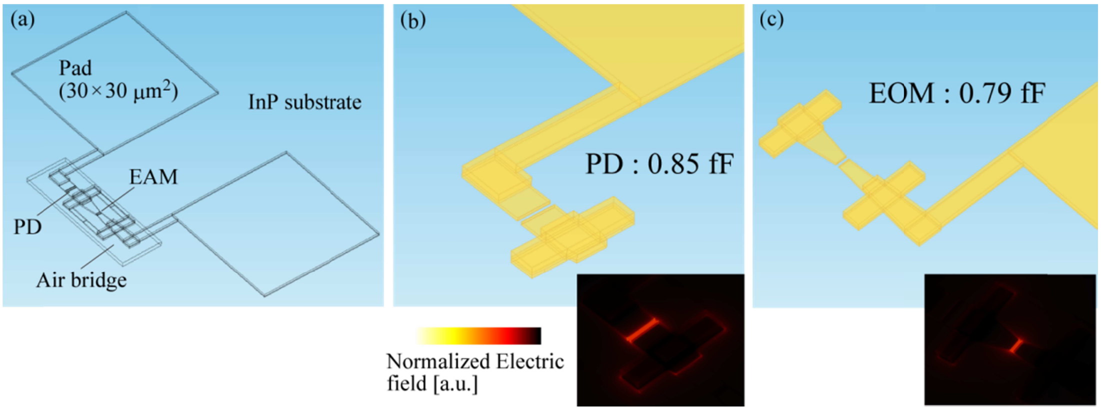

Figure S3 Capacitance of the PD-EOM simulated by the three-dimensional FEM. (a) Simulation model. (b) Capacitance of PD. (c) Capacitance of EOM.

In the PD-EOM, the conversion efficiency from the photocurrent to the voltage, namely transimpedance, is a strict limiting factor as regards the device performance. The frequency response of the transimpedance is determined by the integrated capacitance and the load resistance, and calculated by using the equivalent circuit shown in Figure S4(a). We use a serial resistance for the PD and an EOM of $R_{PD} = R_{EOM} = 1$ kΩ, a load resistance R_{load} of 24 kΩ, an external termination resistance of 50 Ω, and a pad-to-pad capacitance of 5 fF. The analytical expression of the RC bandwidth f_{RC} is approximately given by[9],

$$f_{RC} \approx \frac{1}{2\pi\left[R_{load}\left(C_{PD}+C_{EAM}\right)+R_{PD}C_{PD}\right]}. \tag{S1}$$

The first term of the denominator largely determines f_{RC} as long as $R_{load} >> R_{PD}$. When using C_{PD} = 0.85 fF and C_{EOM} = 0.79 fF, which are obtained by simulating the actual device model (See previous section), the calculated f_{RC} is 3.96 GHz.

We also use the circuit simulator to calculate f_{RC} for the same model as in Figure S4(a) including a large pad-to-pad capacitance. Figure S4(b) shows the frequency response of the transimpedance (V/I), where the integrated capacitance C is changed as a parameter. The 3-dB bandwidth f_{3dB} for $C = C_{PD} + C_{EOM}$ = 2 fF is 3.2 GHz, which agrees well with the experimental result. When we adopt C_{PD} = 0.85 fF and C_{EOM} = 0.79 fF, f_{3dB} = 4.0 GHz. This agrees with the analytical estimation of f_{RC}. This indicates that the large pad-to-pad capacitance does not affect the transimpedance for PD-EOM integration.

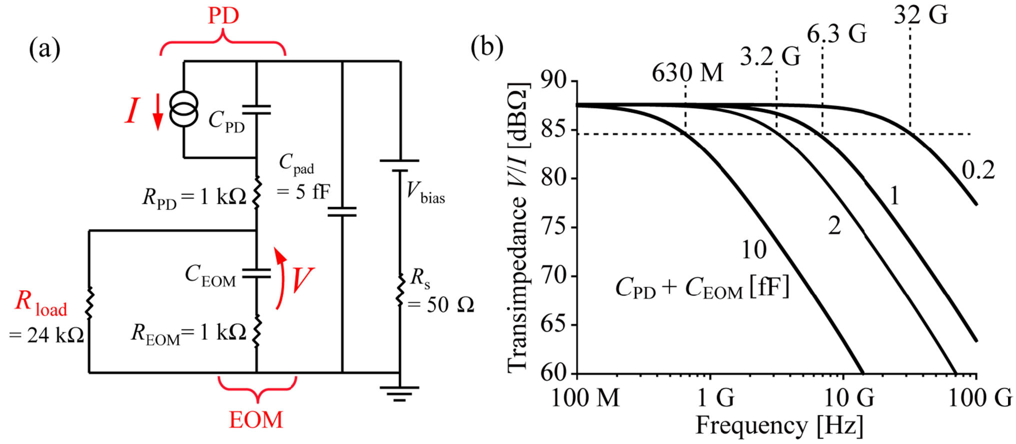

Figure S4 Transimpedance of the PD-EOM circuit. (a) Equivalent circuit and calculation parameters. (b) Calculated transimpedance (V/I) for different capacitances (C_{PD} + C_{EOM}).

5. Isolated PD response

An isolated PhC-PD with a length of 2.6 μm was evaluated. The PD is not connected to the load resistor to evaluate the intrinsic PD characteristics, which are not restricted by the high load resistance and consequent RC time. Figure S5(a) shows the photocurrent spectrum when the input power for the CW light was fixed at 1.1 μW while the wavelength was scanned. A photocurrent was observed over a wide wavelength range in the propagation band of the InGaAs-embedded PhC waveguide. The disappearance of the photocurrent around 1520 nm is due to the cut-off of the input InP-PhC waveguide. The periodic peaks (2 nm interval) appear due to the Fabry-Perot (FP) interference between the waveguide facet end and the input boundary of the PD. In the measurement for PD-EOM integration, we chose one of the FP peak wavelengths, at which the optical responsivity was approximately 1 A/W. Figure S5(b) shows the eye diagram for the intensity-modulated optical signal, which was obtained with the optical peak power increased to 100 μW to allow us to clearly observe the response. We observed eye opening for 20 and 40-Gbit/s NRZ signals generated with a 2^{31}–1 PRBS.

For comparison, the plasmonic detectors are also good candidates for low-*C* PD. Operation bandwidth for the isolated plasmonic PD is up to 100 GHz [10] and is much higher than our PhC-PD, because the RC bandwidth is quite high thanks to the low series resistance. However, for the OEO configuration with load resistor of several tens kΩ, the series resistance of our PhC-PD (~1 kΩ) is dominated by the load resistance. Therefore, the low series resistance does not work so well. The plasmonic PDs have low efficiency due to the metallic optical absorption and poor optical coupling to the plasmonic region. We want to emphasize that it is essentially important to keep high efficiency when reducing the capacitance, which is the main subject of our study. As a consequence, the PhC-PD is better than plasmonic PD in this OEO application.

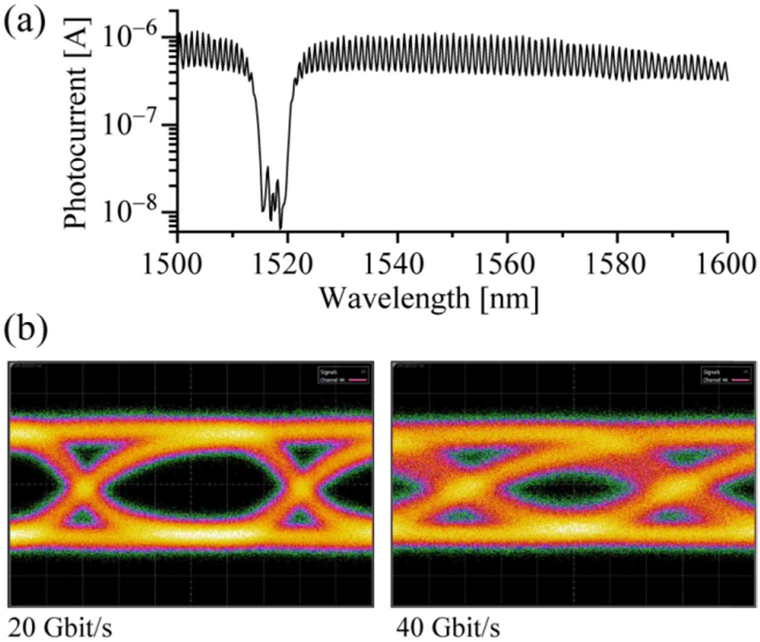

Figure S5 Experimental responses for an isolated PhC-PD without connection to the load resistor. (a) Photocurrent spectrum. The input optical power is 1.1 μW. (b) Eye diagram for 20 and 40 Gbit/s NRZ optical signals. The wavelength and peak power of the input light are set at 1550.0 nm and 100 μW, respectively. The reverse bias voltage is –2 V.

6. Power-dependent light transmission of EOM

The light transmission of the nanocavity EOM depends on the input power because of the optical nonlinearity, and is measured without light injection into the PD, as shown in Figure S6(a). The external reverse bias voltage of –2 V is dominantly applied to the PD due to the resistance of the p-i-n junction being higher than the load resistance. Figure S6(b) shows the transmission spectra for the EOM depending on the input CW optical power. Figure S6(c) and (d) show the output power and transmission, respectively, for the input optical power at a wavelength of 1530.5 nm. Initially, the built-in voltage in the EOM induces optical absorption due to the FKE, and the transmission is as low as –8 dB against the reference waveguide. When increasing the optical power, the photocurrent from the EOM and the high load resistance of 24 kΩ results in a forward voltage across the EOM. This reduces the built-in voltage and suppresses the FKE, and as a result the transmission increases to –3 dB. In the O-E-O operation experiment shown in the main text, we fixed this power condition for the EOM to obtain the lowest insertion loss. When the power is increased further, a resonance redshift caused by the TO nonlinearity occurs in the CW measurement, and thereby the transmission decreases again.

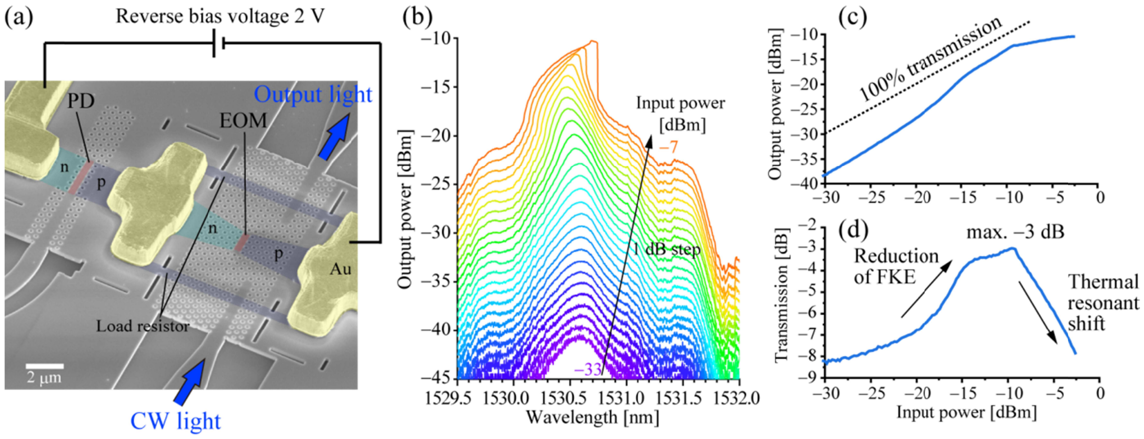

Figure S6 CW light transmission of EOM. (a) Measurement condition. (b) Transmission spectra with different input powers for the EOM. (c) Output power vs input power characteristic. The dashed line denotes the 100% transmission defined by the reference waveguide. (d) Transmission vs input power characteristic. The wavelength is set at 1530.5 nm.

7. Measurement setup for dynamic O-E-O modulation

Figure S7(a) shows the measurement setup. In the eye diagram measurement (Fig. 3b in the main text), an optical signal modulated with an NRZ random pattern and a wavelength of 1550 nm was injected into the PD. The NRZ optical signal with a 2^{11}–1 PRBS frame was repeatedly generated for the modulation. The contrast of this modulation was always kept at more than 10 dB, and hence performed a large-signal operation rather than the small-signal measurement using a network analyzer. A reverse bias voltage of –2 V was applied across the PD-EOM. Since the reverse-biased resistance of the p-i-n junction of the PD is much larger than the parallel circuit of the EOM and the load resistor, this voltage was mostly applied to the PD so that fast carrier extraction was achieved. On the other hand, CW light with its wavelength tuned around the resonance was injected into the EOM. Since the out-coupling loss between the waveguide and the optical fiber is as high as 10.7 ± 0.6 dB, the output signal is amplified with an erbium-doped fiber amplifier (EDFA) and a band-pass filter (BPF). In the observation with a sampling oscilloscope, 32 sampled frames of 2^{11}–1 bits were averaged to exclude the electrical noise of the oscilloscope.

When measuring the frequency response (Fig. 3c in the main text), we used an optical signal modulation with a sinusoidal wave for the same transmitter setup. The output signal from the EOM was detected with an external high-speed PD with a responsivity η_{ref_pd} of 0.65 A/W and a bandwidth of 70 GHz. The RF power of this output signal was evaluated with an RF spectrum analyzer, where the resolution bandwidth (RBW) f_{RBW} was set at 30 Hz and the integral signal power was evaluated. The signal frequency was changed from 150 MHz to 6.5 GHz, and detected the signal power for evaluating the frequency response and 3-dB operation bandwidth.

When measuring the optical conversion efficiency (Fig. 5a and b in the main text), we used the same setup. The signal frequency was fixed to 200 MHz so that the TO effect cannot follow. The conversion efficiency was estimated from the power ratio of the output signal to the input signal. The RF signal power measured from the PhC-PD photocurrent (indicated by blue arrows in Fig. S7a) is given by $(P_{in}\eta_{pd})^2 R_{spe} f_{RBW}$, where P_{in} is on-chip input power for the PhC-PD, η_{pd} (= 1 A/W) is the responsivity of the PhC-PD, R_{spe} (= 50 Ω) is the input resistance of the RF spectrum analyzer. On the other hand, the RF signal power from the PhC-EOM output light (indicated by orange arrows in Fig. S7a) is given by $(P_{out}\eta_{cpl}\eta_{ref\_pd})^2 R_{spe} f_{RBW}$, where P_{out} is on-chip output power from the PhC-EOM, η_{cpl} (= 17.9 ± 0.6 dB) is optical loss including the waveguide-to-fiber out-coupling loss (10.7 ± 0.6 dB) and other optical-component losses up to the external PD. The vertical axis in Fig. 5a in the main text indicates the measured RF signal power from the PhC-EOM output light. On-chip optical input and output powers P_{in} and P_{out}, respectively, are estimated from the measured RF signal power, and the optical signal conversion efficiency was estimated by P_{out}/P_{in}.

Figure S7(b) shows the waveforms observed for the photocurrent and the output signal, which were obtained at the maximum conversion efficiency (η_{conv} = 2.3 ± 0.3) for a normally-on operation. The input peak optical power for the PD is 32 μW, which corresponds to the swing voltage of 1.6 mV observed with the 50-Ω sampling head. On the other hand, the EDFA and BPF are used to observe the output optical signal. The averaged optical power for the output is measured separately, and the coupling loss between the optical fiber and the waveguide (10.7 ± 0.6 dB) is considered to evaluate the on-chip power. As a consequence, the output peak optical power is estimated to be 68 ± 9 μW, and an optical gain of 1.8 – 2.4 is estimated by comparison with the input peak power of 32 μW. This agrees with the signal conversion efficiency estimated with the RF signal power measurement described above.

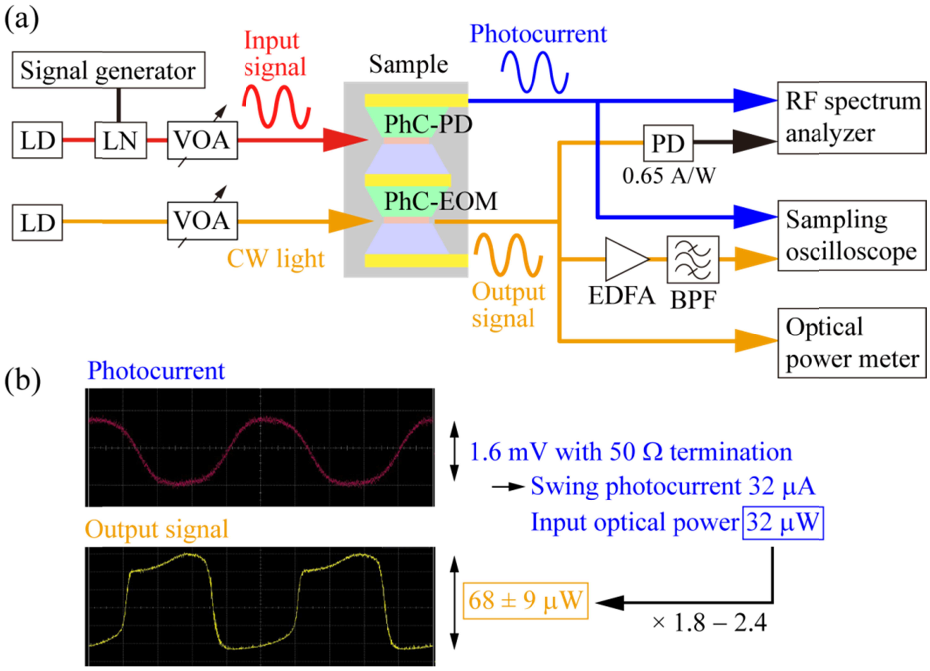

Figure S7 Measurement of AC responses in oscilloscope. (a) Measurement setup. (b) Observed photocurrent and output signal light waveforms. The maximum conversion efficiency (2.3 ± 0.3) for a normally-on operation is shown (See Fig. 5b in main text).

8. Time-of-flight pulse delay measurement

We tried to evaluate the carrier transit-time bandwidth by using a time-of-flight short-pulse measurement. The difference between the NRZ response and the impulse response has been reported in Ref. 11. The rise and fall time for the NRZ response such as Fig. 3b in the main text are both limited by RC. On the other hand, the rise time of the impulse response is determined by the quick charging of circuit capacitance (so it is limited by carrier-transit time from the absorber), while the RC limits the fall time. The quasi-impulse response and the signal delay limited by the carrier transit time for the

O-E-O transistor were measured with the time-of-flight technique. An optical pulse with a width of 14 ps was injected into the PD, while CW light with a wavelength of the normally-off condition (1530.6 nm) was injected into the EOM, as shown in Figure S8(a). The output pulse from the EOM was observed with the sampling oscilloscope. We evaluated the pulse delay τ for the O-E-O transistor by comparing this pulse with the output pulse observed for the reference waveguide. Figure S8(b) shows measured waveforms with normalized intensities. The estimated delay is τ = 25 ps. The rise time of the output waveform should be mainly determined by the carrier transit time in the PD rather than the RC time, because the capacitance of O-E-O transistor circuit is instantaneously charged and the EOM is driven when the photo-generated carriers are extracted into the circuit. The operation bandwidth limited by the carrier transit time [12] would therefore be $f_{TR} = 0.45/\tau = 18$ GHz. The total bandwidth including the RC-limited bandwidth f_{RC} is given by $f_{total} = (f_{TR}^{-2} + f_{RC}^{-2})^{-0.5}$, and was estimated to be 3.3 GHz in Fig. 3 in the main text. Therefore, the f_{TR} (18 GHz) hardly affects f_{total}, while the f_{RC} (3.4 GHz) has a dominant effect.

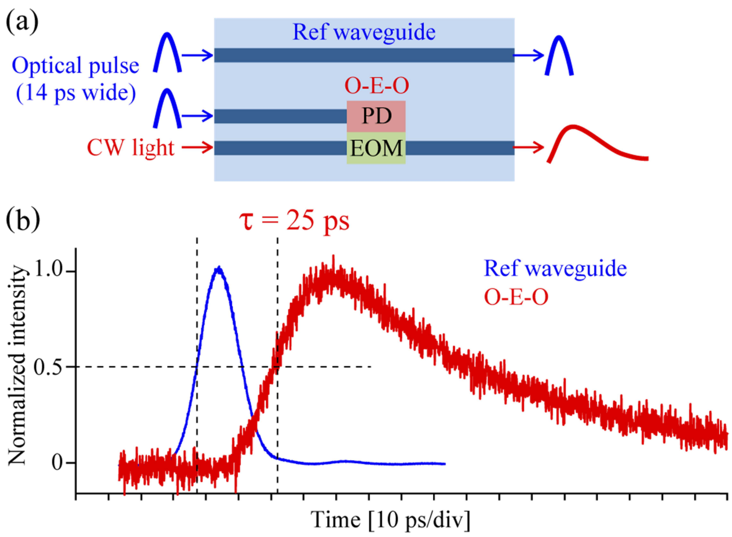

Figure S8 Time-of flight measurement of optical pulse delay.

9. Picosecond pulse response

Observation of the short-pulse response can also be used for a second check of device capacitance. The capacitance is instantaneously charged by the optical pulse via the PD, and the pulse energy is used to evaluate the dynamic charge ΔQ and the photovoltage

V_{pho}, and consequently $C = \Delta Q/V_{pho}$. In this measurement, 2-ps-wide optical pulses with a center wavelength of 1550 nm and CW light are injected into the PD and the EOM, respectively. Figure S9(a) shows the transient response of the EOM output light, and Figure S9(b) shows the photocurrent response, which is detected with the 50-Ω sampling oscilloscope head. The extinction ratio for the output light is plotted in Figure S9(c). If we take the same extinction ratio (1.5 dB) as the NRZ modulation in Fig. 3b in the main text, E_{pulse} is as low as 1.9 ± 0.2 fJ, thus contributing to the dynamic charge of ΔQ = 1.9 ± 0.2 fC with a responsivity η_{pd} = 1 A/W. Figure S9(d) shows the instantaneous photovoltage V_{pho} estimated by multiplying the peak photocurrent and R_{load} = 24 kΩ. A V_{pho} as high as 0.71 ± 0.08 V is obtained for the same E_{pulse}. Finally, $\Delta Q/V_{pho} = \eta_{pd}E_{pulse}/V_{pho}$ is plotted in Figure S9(e). This remains almost constant below the PD saturation limit (V_{pho} < 1 V), thereby indicating that C = 2.0–2.6 fF. This capacitance agrees with the estimation obtained from the RC bandwidth discussed in the main text.

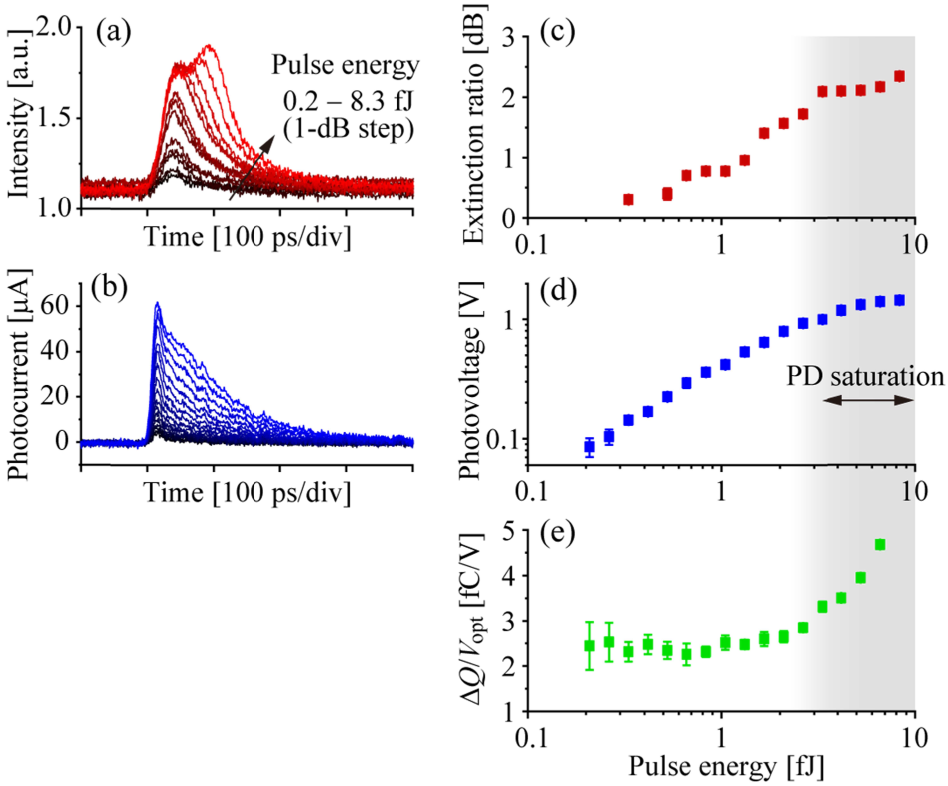

Figure S9 Short pulse response. (a) Output signal for normally-on operation. (b) Photocurrent response. The optical pulse energy E_{pulse} is changed from 0.2 to 8.3 fJ. (c) Extinction ratio, (d) Photovoltage V_{pho} across the load resistor. (e) Charge over photovoltage ($\Delta Q/V_{pho}$) estimated for the optical pulse energy for the PD. The shaded area denotes the saturation region of the PD.

10. Performance comparison as photoreceiver

The O-E-O device includes conversion from optical energy to voltage, and therefore our experimental results provide a benchmark for a photoreceiver. The resistor-loaded receiver comprises a PD and a serial load resistor, and an EOM is used for optical probing the generated voltage. The light-to-voltage conversion efficiency for the resistor-loaded receiver would be $\eta_{LV} = V_{pho}/P_{in} = \eta_{pd}R_{load}$ [V/W]. On the other hand, the 3-dB bandwidth (assuming the RC limited) $f_{3dB} = f_{RC} = (2\pi CR_{load})^{-1}$. These two values have a trade-off relationship. The efficiency-bandwidth product (EBP) is given by $\eta_{LV}f_{3dB} \sim \eta_{pd}(2\pi C)^{-1}$ and hence is limited by the capacitance for the fixed η_{pd} = 1 A/W. Figure S10(a) shows the η_{LV} and f_{3dB} mapping, where the total capacitance C is changed as a parameter. The figure also plots previously reported values for Ge photoreceivers integrated with a Si-CMOS transimpedance amplifier (TIA)/limiting amplifier (LA) circuit[13-18] and InGaAs-based photoreceivers integrated with an InP-based heterojunction bipolar transistor (HBT)/ high electron mobility transistor (HEMT) circuit[19-24]. This indicates that a resistor-loaded PD with a fF-capacitance has an EBP value comparable to those of most CMOS receivers. The conventional receivers support the high EBP thanks to the integrated amplifiers. However, it should be noted that such amplifiers also consume a huge amount of electric energy at the pJ/bit level, and this dominates the overall energy consumption. Figure S10(b) summarizes the energy consumption of the EBP in these receivers. The performance in our previous work on PD-resistor integration was limited by a parasitic capacitance of more than 10 fF due to the use of metal wiring[25]. This problem is solved in the present work. Our resistor-loaded PD consumes an electrical energy of 3.2 fJ/bit as a result of the energy dissipation induced by the photocurrent and the reverse bias voltage. This ensures that our receiver has a similar EBP performance to conventional receivers but has a remarkably low total energy consumption of only 4.8 fJ/bit.

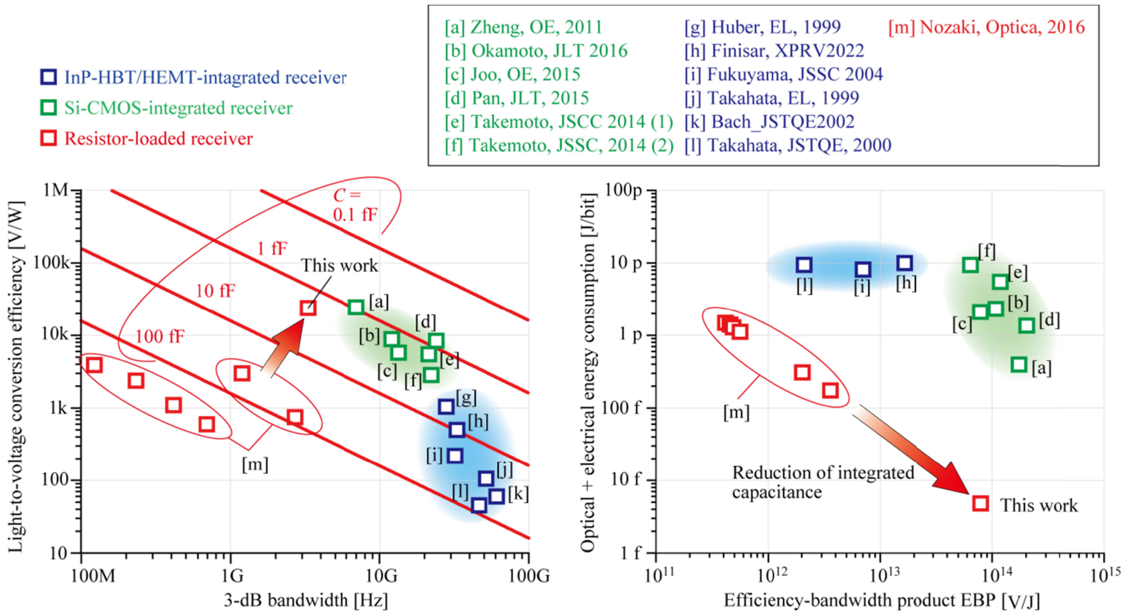

Figure S10 Performance comparison as photoreceiver. (a) Light-to-voltage conversion efficiency vs 3-dB bandwidth. The red lines show calculated results for a resistor-loaded receiver, in which the total capacitance *C* is changed as a parameter. The plots also show reported values for Si-CMOS-integrated photoreceivers (green) and InP-based HBT/HEMT-integrated photoreceivers (blue). (b) Optical + electrical energy consumption vs EBP.

11. Operation bandwidth for normally-on/-off operation

Figure S11 shows the frequency responses and eye diagrams for normally-on/-off operations. As shown in the main text, the normally-off operation exhibits f_{3dB} = 3.3 GHz, a 10-Gbit/s eye diagram, and an optical conversion efficiency of 0.6. On the other hand, the normally-on operation limits the f_{3dB} to 900 MHz (η_{conv} = 2.3) and 2.0 GHz (η_{conv} = 1.2), depending on the light wavelength and the subsequent conversion efficiency. A steep roll-off is observed in the frequency responses for the normally-on operation. A possible explanation is as follows. For the normally-off operation, optical absorption and carrier generation in the EOM occur when a photovoltage is applied by the PD (the input optical bit for the PD is “1”). The photovoltage quickly extracts the carriers and hence the speed of the overall O-E-O operation is not limited by the carrier traveling time but only by the RC time. On the other hand, for the normally-on operation, the optical absorption and carrier generation occur at a time when there is no input for the PD (the input optical bit for the PD is “0”). In this situation, the carriers in the EOM are not quickly extracted, and consequently the space charge effect would make the operation speed slow. This will be solved by replacing the embedded InGaAsP with that having a shorter absorption wavelength to reduce carrier generation in the EOM and operate dominantly with a refractive index modulation.

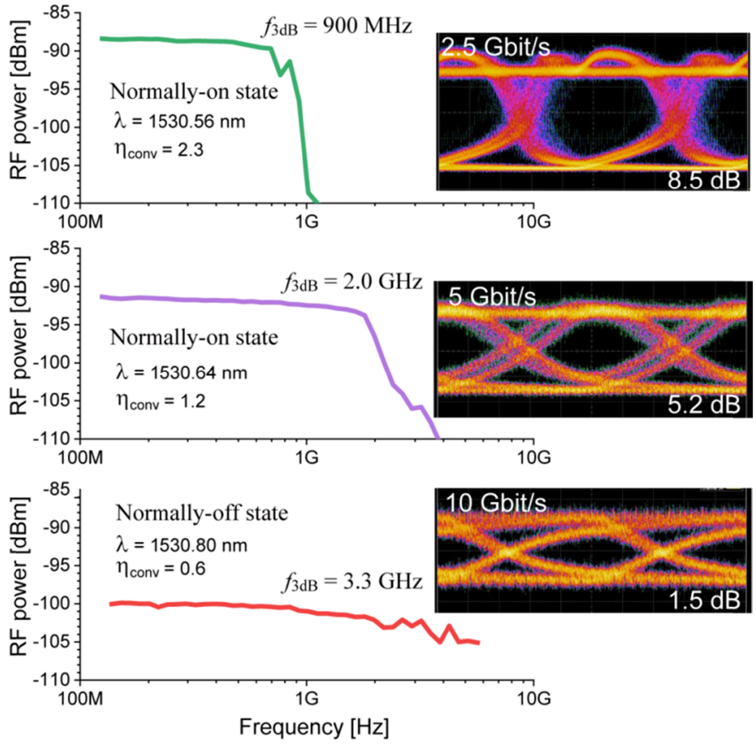

Figure S11 Frequency responses for normally-on and normally-off states. Eye diagrams are shown for an NRZ signal with 2^{11}-1 PRBS bits.

12. Performance comparison as all-optical nonlinear switch

The O-E-O device can work as an all-optical nonlinear switch. Figure S12 compares various all-optical switches in terms of their switching energy per bit and switching time. Gray lines indicate the contour lines given by the product of the switching energy and the switching time. The product was largely limited to around 10^{-24}–10^{-22} for previous optical switches except for the PhC cavity switches. It is clearly seen that our O-E-O switch can operate with more than two orders of magnitude less energy than previously-reported O-E-O switches[26-28]. The energy-time product of 2.3×10^{-25} for our O-E-O is also two orders of magnitude lower than previous switches, which is attributed to the low integrated capacitance. One of the PhC cavity switches has sub-fJ/bit switching energy[29], which is the only switch with a lower switching energy than our present O-E-O device. The integrated capacitance is at present determined by the electrical components such as the p/n doping regions and metal wiring. If we look at the device photograph in Fig. 2(a), there is still room to further miniaturize these components and thus reduce the capacitance while maintaining the O-E-O functions. This should reduce the energy-time product to the 10^{-26} level.

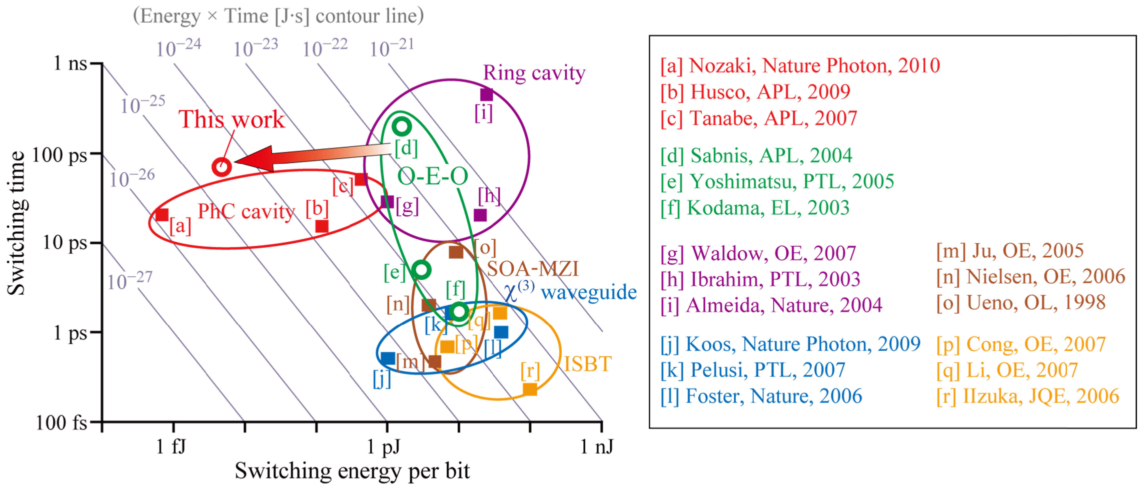

Figure S12 Performance comparison as all-optical nonlinear switch. Switching time vs. switching energy is shown for various on-chip switches. The plots show reported values for PhC cavities[29-31], O-E-O switches[26-28], Ring cavities[32-34], $\chi^{(3)}$ waveguides[35-37], SOA-MZIs[38-40], and Inter-sub-band transition (ISBT) switches[41-43].

13. Total energy consumption and efficiency for O-E-O transistor

We estimated the total energy consumption, the transferred optical energy, and the total efficiency for the O-E-O transistor action. When the input optical energy for the PD is $E_{\mathrm{opt\_PD}}$, the electrical energy consumption due to the photocurrent energy dissipation E_{elect} is given by $E_{\mathrm{opt\_PD}}\eta_{\mathrm{pd}}V_{\mathrm{bias}}$, where η_{pd} is the optical responsivity and V_{bias} is the reverse bias voltage. We also consider the input CW light for the EOM, and its optical energy $E_{\mathrm{opt\_EOM}}$ is estimated by the CW light power and the operation bit rate. Accordingly, the total energy consumption is given by $E_{\mathrm{total}} = E_{\mathrm{opt\_PD}} + E_{\mathrm{opt\_PD}} + E_{\mathrm{elect}}$. On the other hand, the transferred optical energy by the O-E-O transistor is given by $E_{\mathrm{trans}} = \eta_{\mathrm{conv}}E_{\mathrm{opt\_PD}}$, where η_{conv} is the optical signal conversion efficiency. Consequently, the total efficiency for transferring the optical signal is defined by $\eta_{total} = E_{trans}/E_{total}$. Here we estimated these figures for the normally-off and normally-on conditions as follows.

(1) Normally-off condition operating at a bit rate of 10 Gbit/s

E_{opt_PD} = 1.6 fJ/bit

E_{elect} = 3.2 fJ/bit for η_{pd} = 1 A/W and V_{bias} = 2 V

E_{opt_EOM} = 16.7 ± 3.8 fJ/bit for 10 Gbit/s

E_{total} = 21.5 ± 3.8 fJ/bit

E_{trans} = 0.95 ± 0.15 fJ/bit for η_{conv} = 0.6 ± 0.1

η_{total} = 4.4 ± 0.1 %

(2) Normally-on condition operating at a bit rate of 2.5 Gbit/s

E_{opt_PD} = 6.4 fJ/bit

E_{elect} = 12.8 fJ/bit for η_{pd} = 1 A/W and V_{bias} = 2 V

E_{opt_EOM} = 40.9 ± 5.7 fJ/bit for 2.5 Gbit/s

E_{total} = 60.1 ± 5.7 fJ/bit

E_{trans} = 14.7 ± 1.9 fJ/bit for η_{conv} = 2.3 ± 0.3

η_{total} ~ 24.4 ± 0.8 %

η_{total} for the normally-on is higher than that for the normally-off. This comes from larger extinction during the EO modulation of the resonant transmission (See Fig. 2d in the main text). Larger η_{total} will be expected by replacing the embedded InGaAsP in the EOM with that with a shorter absorption wavelength to operate dominantly with an index modulation in the transparent region, because this will suppress the absorption loss in the EOM.

References

1. Kuramochi, E. et al. Ultralow bias power all-optical photonic crystal memory realized with systematically tuned L3 nanocavity. *Appl. Phys. Lett.* **107**, 221101 (2015).
2. Kuramochi, E. et al. Large-scale integration of wavelength-addressable all-optical memories in a photonic crystal chip. *Nat. Photon.* **8**, 474-481 (2014).
3. Matsuo, S. et al. Ultralow Operating Energy Electrically Driven Photonic Crystal Lasers. *IEEE J. Sel. Top. Quantum Electron.* **19**, 4900311 (2013).
4. Miller, D.A.B. Energy consumption in optical modulators for interconnects. *Opt. Express* **20**, A293-A308 (2012).

5. Timurdogan, E. et al. An ultralow power athermal silicon modulator. *Nat. Commun.* **5**, 4008 (2014).
6. Koeber, S. et al. Femtojoule electro-optic modulation using a silicon-organic hybrid device. *Light-Sci. Appl.* **4**, e255 (2015).
7. Nozaki, K. et al. Ultralow-energy electro-absorption modulator consisting of InGaAsP-embedded photonic-crystal waveguide. *APL Photon.* **2**, 056105 (2017).
8. Sabnis, V.A. et al. Intimate monolithic integration of chip-scale photonic circuits. *IEEE J. Sel. Top. Quantum Electron.* **11**, 1255-1265 (2005).
9. Nozaki, K. et al. Sub-fF-capacitance photonic-crystal photodetector towards fJ/bit on-chip receiver. *IEICE Trans. Electron.* **E100-C**, 750-758 (2017).
10. Salamin, Y. et al. 100 GHz Plasmonic Photodetector. *Acs Photonics* **5**, 3291-3297 (2018).
11. Boivin, L., Nuss, M.C., Shah, J., Miller, D.A.B. & Haus, H.A. Receiver sensitivity improvement by impulsive coding. *IEEE Photon. Tech. Lett.* **9**, 684-686 (1997).
12. Bowers, J.E. & Burrus, C.A. Ultrawide-Band Long-Wavelength P-I-N Photodetectors. *J. Lightwave Technol.* **5**, 1339-1350 (1987).
13. Okamoto, D. et al. A 25-Gb/s 5 x 5 mm(2) Chip-Scale Silicon-Photonic Receiver Integrated With 28-nm CMOS Transimpedance Amplifier. *J. Lightwave Technol.* **34**, 2988-2995 (2016).
14. Joo, J. et al. Silicon photonic receiver and transmitter operating up to 36 Gb/s for lambda similar to 1550 nm. *Opt. Express* **23**, 12232-12243 (2015).
15. Takemoto, T. et al. A 25-Gb/s 2.2-W 65-nm CMOS Optical Transceiver Using a Power-Supply-Variation-Tolerant Analog Front End and Data-Format Conversion. *IEEE J. Solid-St. Circ.* **49**, 471-485 (2014).
16. Zheng, X.Z. et al. Ultra-efficient 10Gb/s hybrid integrated silicon photonic transmitter and receiver. *Opt. Express* **19**, 5172-5186 (2011).
17. Pan, Q. et al. A 30-Gb/s 1.37-pJ/b CMOS Receiver for Optical Interconnects. *J. Lightwave Technol.* **33**, 778-786 (2015).
18. Takemoto, T. et al. A 25-to-28 Gb/s High-Sensitivity (-9.7 dBm) 65 nm CMOS Optical Receiver for Board-to-Board Interconnects. *IEEE J. Solid-St. Circ.* **49**, 2259-2276 (2014).
19. Fukuyama, H. et al. Photoreceiver module using an InP HEMT transimpedance amplifier for over 40 Gb/s. *IEEE J. Solid-St. Circ.* **39**, 1690-1696 (2004).
20. Huber, A. et al. Monolithic, high transimpedance gain (3.3 k Omega), 40 Gbit s InP-HBT photoreceiver with differential outputs. *Electron. Lett.* **35**, 897-898 (1999).

21. Takahata, K., Muramoto, Y., Fukano, H. & Matsuoka, Y. 52GHz bandwidth monolithically integrated WGPD/HEMT photoreceiver with large O/E conversion factor of 105V/W. *Electron. Lett.* **35**, 1639-1640 (1999).
22. Finisar. https://www.finisar.com/communication-components/xprv2022a
23. Bach, H.G., Beling, A., Mekonnen, G.G. & Schlaak, W. Design and fabrication of 60-Gb/s InP-based monolithic photoreceiver OEICs and modules. *IEEE J. Sel. Top. Quantum Electron.* **8**, 1445-1450 (2002).
24. Takahata, K. et al. Ultrafast monolithic receiver OEIC composed of multimode waveguide p-i-n photodiode and HEMT distributed amplifier. *IEEE J. Sel. Top. Quantum Electron.* **6**, 31-37 (2000).
25. Nozaki, K. et al. Photonic-crystal nano-photodetector with ultrasmall capacitance for on-chip light-to-voltage conversion without an amplifier. *Optica* **3**, 483-492 (2016).
26. Sabnis, V.A. et al. Optically controlled electroabsorption modulators for unconstrained wavelength conversion. *Appl. Phys. Lett.* **84**, 469-471 (2004).
27. Kodama, S., Yoshimatsu, T. & Ito, H. 320 Gbit/s error-free demultiplexing using ultrafast optical gate monolithically integrating a photodiode and electroabsorption modulator. *Electron. Lett.* **39**, 1269-1270 (2003).
28. Yoshimatsu, T., Kodama, S., Yoshino, K. & Ito, H. 100-Gb/s error-free wavelength conversion with a monolithic optical gate integrating a photodiode and electroabsorption modulator. *IEEE Photon. Tech. Lett.* **17**, 2367-2369 (2005).
29. Nozaki, K. et al. Sub-femtojoule all-optical switching using a photonic-crystal nanocavity. *Nat. Photon.* **4**, 477-483 (2010).
30. Husko, C. et al. Ultrafast all-optical modulation in GaAs photonic crystal cavities. *Appl. Phys. Lett.* **94**, 021111 (2009).
31. Tanabe, T. et al. Fast all-optical switching using ion-implanted silicon photonic crystal nanocavities. *Appl. Phys. Lett.* **90**, 031115 (2007).
32. Waldow, M. et al. 25ps all-optical switching in oxygen implanted silicon-on-insulator microring resonator. *Opt. Express* **16**, 7693-7702 (2008).
33. Ibrahim, T.A. et al. All-optical switching in a laterally coupled microring resonator by carrier injection. *IEEE Photon. Tech. Lett.* **15**, 36-38 (2003).
34. Almeida, V.R., Barrios, C.A., Panepucci, R.R. & Lipson, M. All-optical control of light on a silicon chip. *Nature* **431**, 1081-1084 (2004).
35. Koos, C. et al. All-optical high-speed signal processing with silicon-organic hybrid slot waveguides. *Nat. Photon.* **3**, 216-219 (2009).
36. Pelusi, M.D. et al. Ultra-high Nonlinear As2S3 planar waveguide for 160-Gb/s

optical time-division demultiplexing by four-wave mixing. *IEEE Photon. Tech. Lett.* **19**, 1496-1498 (2007).

37. Foster, M.A. et al. Broad-band optical parametric gain on a silicon photonic chip. *Nature* **441**, 960-963 (2006).
38. Ju, H. et al. SOA-based all-optical switch with subpicosecond full recovery. *Opt. Express* **13**, 942-947 (2005).
39. Nielsen, M.L., Mork, J., Suzuki, R., Sakaguchi, J. & Ueno, Y. Experimental and theoretical investigation of the impact of ultra-fast carrier dynamics on high-speed SOA-based all-optical switches. *Opt. Express* **14**, 331-347 (2006).
40. Ueno, Y., Nakamura, S. & Tajima, K. Record low-power all-optical semiconductor switch operation at ultrafast repetition rates above the carrier cutoff frequency. *Opt. Lett.* **23**, 1846-1848 (1998).
41. Cong, G.W., Akimoto, R., Akita, K., Hasama, T. & Ishikawa, H. Low-saturation-energy-driven ultrafast all-optical switching operation in (CdS/ZnSe)/BeTe intersubband transition. *Opt. Express* **15**, 12123-12130 (2007).
42. Li, Y., Bhattacharyya, A., Thomidis, C., Moustakas, T.D. & Paiella, R. Ultrafast all-optical switching with low saturation energy via intersubband transitions in GaN/AlN quantum-well waveguides. *Opt. Express* **15**, 17922-17927 (2007).
43. Iizuka, N., Kaneko, K. & Suzuki, N. All-optical switch utilizing intersubband transition in GaN quantum wells. *IEEE J. Quantum Electron.* **42**, 765-771 (2006).